AGU PUBLICATIONS

Journal of Advances in Modeling Earth Systems

RESEARCH ARTICLE
10.1002/2015MS000572

Resolution and domain-size sensitivity in implicit large-eddy simulation of the stratocumulus-topped boundary layer

Jesper G. Pedersen[1], Szymon P. Malinowski[1], and Wojciech W. Grabowski[2]

[1]Faculty of Physics, Institute of Geophysics, University of Warsaw, Warsaw, Poland, [2]National Center for Atmospheric Research, Boulder, Colorado, USA

Key Points:
- Influence of domain size and vertical and horizontal resolution in ILES of the STBL is investigated
- Flat anisotropic gridboxes lead to better agreement with DYCOMS-II measurements than isotropic boxes
- The size of the computational domain is found to have no significant impact on cloud statistics

Supporting Information:
- Supporting Information S1

Correspondence to:
J. G. Pedersen,
jesper@igf.fuw.edu.pl

Citation:
Pedersen, J. G., S. P. Malinowski, and W. W. Grabowski (2016), Resolution and domain-size sensitivity in implicit large-eddy simulation of the stratocumulus-topped boundary layer, *J. Adv. Model. Earth Syst.*, *8*, 885–903, doi:10.1002/2015MS000572.

Received 23 OCT 2015
Accepted 8 MAY 2016
Accepted article online 11 MAY 2016
Published online 4 JUN 2016

Abstract As a complement to measurements, numerical modeling facilitates improved understanding of the complex turbulent processes in the stratocumulus-topped boundary layer (STBL). Due to limited computational resources simulations are often run at too coarse resolutions to resolve details of cloud-top turbulence and potentially in computational domains too small to account for the largest scales of boundary layer circulations. The effects of such deficiencies are not fully understood. Here the influence of resolution/anisotropy of the computational grid and domain size in under-resolved implicit large-eddy simulation of the STBL is investigated. The performed simulations are based on data from the first research flight of the DYCOMS-II campaign. Regarding cloud cover and domain-averaged liquid water path, simulations with horizontal/vertical grid spacing of 35/5 m, 70/10 m, and 105/15 m are found to agree better with measurements than more computationally expensive simulations with isotropic grid boxes, e.g., with 10/10 m or 15/15 m grid spacing. While decreasing the vertical grid spacing allows more representative simulation of the thin, turbulent, stably stratified interfacial layer between the STBL and the free troposphere, coarsening the horizontal resolution dampens vertical velocity fluctuations in this region and mimics the observed anisotropy of stably stratified small-scale turbulence near the cloud top. The size of the computational domain is found to have almost no impact on mean cloud properties. However, increasing it from $3.5\times3.5\,\mathrm{km}^2$ to 14×14 km^2 does lead to the occurrence of larger coherent updraft structures. Increasing it further to $21\times21\,\mathrm{km}^2$ shows little or no increase in the updraft size.

1. Introduction

Understanding processes behind the formation, maintenance and dissipation of stratocumulus clouds is essential for climate and weather prediction. In situ measurements of the cloud-top structure [*Stevens et al.*, 2003; *Gerber et al.*, 2013] provide valuable insights, but the knowledge of key aspects such as entrainment of dry air from the free atmosphere into the cloud is still incomplete.

Numerical simulations complement measurements [e.g., *Stevens et al.*, 2005], but are often under-resolved and/or confined to computational domains too small to account for the largest relevant structures of the flow due to limited computational resources and the wide range of spatial scales involved. *de Roode et al.* [2004] argue that large domains (tens of kilometres) are necessary to model stratocumulus clouds. *Yamaguchi et al.* [2013] show dependence of turbulence intensity on the domain size. According to *Wood* [2012], the typical aspect ratio of closed mesoscale convective cells in the stratocumulus-topped boundary layer (STBL) is between 3 and 40. For low marine clouds in general, *Wood and Hartmann* [2006] show that mesoscale cellular convection is very common in boundary layers deeper than ∼800 m, and that the characteristic cell length is 30–40 times the boundary layer depth. Thus, with a boundary layer depth of ∼1 km, a computational domain with a horizontal extent of $\mathcal{O}(100)\times\mathcal{O}(100)\,\mathrm{km}^2$ would be required, at least for the STBL over a uniform surface, like the ocean. Combining such a horizontal domain with a computational grid sufficiently fine to resolve the smallest eddies involved in the entrainment process is not yet feasible. Numerical modeling reported in *de Lozar and Mellado* [2013, 2015] shows that scales relevant for entrainment are between ∼0.5 and ∼60 m. This supports the experimental finding by *Malinowski et al.* [2013] of a fine multilayer structure of the Entrainment Interfacial Layer (EIL) capping the stratocumulus top. As a result, the outcome of numerical simulations is in many cases dependent on the resolution [see e.g., *Stevens et al.*, 2005; *Yamaguchi and Randall*, 2012; *Cheng et al.*, 2010] and/or domain size [*de Roode et al.*, 2004]. Here we

investigate how changes in the horizontal and vertical resolution, and the domain size affect outcomes of implicit large-eddy simulation (ILES) of the STBL. Our primary aim is to explain and verify tendencies observed in earlier studies. We approach this by performing a wide range of simulations systematically varying horizontal and vertical grid spacing as well as domain size.

ILES differs from traditional large-eddy simulation (LES) in the sense that the effect of unresolved turbulence is included implicitly through truncation terms of the applied numerical scheme, and not through an explicit subgrid-scale (SGS) model. In particular a class of nonoscillatory finite-volume (NFV) schemes have proven to be well-suited for this type of modeling. A number of such schemes as well as the requirements for successful ILES are discussed in *Grinstein et al*. [2007]; the appearance and leading order of dissipative truncation terms are shown to be key properties. To provide a rationale for the successful use of NFV schemes in ILES, *Margolin and Rider* [2002] show through modified equation analysis, that a specific NFV scheme—the Multidimensional Positive definite Advection Transport Algorithm (MPDATA) [*Smolarkiewicz*, 1984] as used in the present study—applied to describe Burgers' fluid, resembles an analytical finite-volume form of the governing equation, and that the need for an explicit SGS model thereby is removed. *Grinstein et al*. [2007] extend the analysis to the 2-D Navier-Stokes equation and come to similar conclusions. They also show that not all NFV schemes are suitable for ILES. The theory behind the method is still being developed, and as noted by e.g., *Domaradzki et al*. [2003] the interest in ILES is partly due to the absence of a universal and clearly superior explicit SGS model based on physical principles.

Our choice to use ILES for simulation of the STBL is motivated by the findings of *Stevens et al*. [2005] who compare STBL-simulations based on research flight 1 (RF01) of the DYCOMS-II campaign [*Stevens et al*., 2003] from a number of different LES models and model setups. The comparison shows that simulations with no explicit SGS model for the scalar variables agree better with measurements than those employing an explicit SGS model. Turning off the SGS model produces a thicker and more horizontally homogeneous cloud layer in better agreement with observations. *Kurowski et al*. [2009, 2010] also simulate the RF01 DYCOMS-II case and obtain similar results; the SGS-scheme sensitivity study in *Kurowski et al*. [2010] shows that ILES—the simulation with no explicit SGS model for either scalar variables or velocity components—compares better to experimental results in terms of cloud cover and liquid water path (LWP) than simulations with explicit SGS terms included.

Piotrowski et al. [2009] simulate the dry convective boundary layer using a range of numerical setups, and find that ILES captures the influence of unresolved scales of motion on the resolved scales better than conventional LES. In simulations of the Taylor-Green vortex and of homogeneous stratified turbulence *Remmler and Hickel* [2012] show good agreement between direct numerical simulation and ILES. These findings serve as further motivation for the use of ILES in the present study. Yet another motivation is related to the finding of *Piotrowski et al*. [2009] that the ability of LES to reproduce the spatial structure of convective circulations in the boundary layer depends on the effective viscosities in the horizontal and vertical directions. In the virtual reality of the numerical simulation, these effective viscosities depend on the numerical scheme and filtering applied, the SGS scheme in LES, and last but not least on the size and the aspect ratio (width-to-height ratio) of the gridboxes. In ILES, with no filtering and no SGS scheme only the properties of numerics and grid are of relevance. Finally we note that *Piotrowski et al*. [2009] find that realistic results requires a domain extending $\mathcal{O}(10)\times\mathcal{O}(10)\,\mathrm{km}^2$ in the horizontal directions resolved with $\mathcal{O}(10)\times\mathcal{O}(10)$ m^2 grid intervals.

In the RF01 DYCOMS-II case, *Stevens et al*. [2005] find that decreasing the vertical grid spacing from 10 to 1 m in the cloud top region increases the LWP, while changing the horizontal grid spacing from 35 to 20 m has no significant impact on the statistics of the flow in the computational domain of $\sim 3.4\times 3.4\times 1.5\,\mathrm{km}^3$. *Kurowski et al*. [2009] find that in simulations applying the TKE-based SGS model and a horizontal grid spacing of 35 m, both the cloud cover and LWP increase with refinement of the vertical grid spacing from 10 to 2.5 m. However, applying ILES and 5 m vertical grid spacing resulted in a significantly larger cloud cover and LWP (see Table A.I therein). *Yamaguchi and Randall* [2012] perform large-eddy simulations based on the same data, primarily to study cooling of entrained air parcels in detail. Their results indicate sensitivity to both horizontal and vertical grid spacing, as well as to the way surface fluxes and longwave radiation is modeled. While the studies mentioned above use anisotropic gridboxes, *Matheou and Chung* [2014] simulate the RF01 DYCOMS-II case using the so-called buoyancy-adjusted stretched-vortex SGS model [*Chung*

and Matheou, 2014] and isotropic gridboxes; they find that decreasing the grid spacing in all three directions from 10 to 2.5 m leads to higher cloud cover and LWP.

Other studies of resolution and domain-size sensitivity in LES, include *Stevens et al*. [2002] who investigate the case of shallow cumulus convection with an overlying stratocumulus layer. With a fixed grid aspect ratio of 2:1, cloud cover fraction, LWP, and inversion rise rate are found to increase with higher resolution (decreasing Δx from 80 m to 20 m), and the mean profiles of the water vapour mixing ratio and liquid water potential temperature to depend more clearly on the resolution than on the domain size, with the horizontal extent changing from 6.5 to 20 km in both directions. *Cheng et al*. [2010] simulate a range of different boundary-layer cloud cases at coarse resolutions, and generally find—in agreement with *Yamaguchi and Randall* [2012]—that cloud cover and LWP decrease with refinement of the horizontal resolution, but increase with refinement of the vertical resolution. We note that these tendencies are observed in multiple studies, including most of those mentioned here, with the results of *Stevens et al*. [2002] and *Matheou and Chung* [2014] indicating stronger sensitivity to changes in the vertical grid spacing than to changes in the horizontal directions. The lack of sensitivity to horizontal resolution reported by *Stevens et al*. [2005] diverge from the other studies, and we will come back to this later in the text.

In LES of a dry daytime convective atmospheric boundary layer, *Sullivan and Patton* [2011] find a resolution of 20 m in the horizontal directions and 8 m in the vertical sufficient for convergence. They emphasize the need for sufficiently small vertical grid spacing to resolve the capping inversion while still maintaining reasonable grid aspect ratios (in the specific case $\Delta x/\Delta z=2.5$). The length scale in the eddy-viscosity SGS model applied in their simulations (following *Deardorff* [1980] as well as in other Smagorinsky-type models) is defined as a combination of the vertical and horizontal grid spacing, making its validity in simulations with anisotropic grids questionable. The impact of the choice of SGS length scale in simulations of moist deep convection is shown by *Kurowski et al*. [2014, Figure 8], and in simulation of the dry planetary boundary layer by *Nishizawa et al*. [2015]. In ILES, there is no need for an explicitly specified SGS length scale. *Khani and Waite* [2014, 2015] investigate idealized stratified turbulence in a triply periodic cubic domain and find the classic Smagorinsky SGS model [*Smagorinsky*, 1963] to work poorly; better performance—in the sense that fewer grid points are needed for physically accurate results—is obtained with the dynamic Smagorinsky model [*Germano et al*., 1991]. *Basu and Porté-Agel* [2006] show promising results using a dynamic SGS model as well. Here however, we rely on the simpler and faster method of ILES, primarily motivated by the aforementioned studies by *Stevens et al*. [2005], *Piotrowski et al*. [2009], *Kurowski et al*. [2009, 2010], and *Remmler and Hickel* [2012]. Reduced simulation time and no need to specify an explicit SGS length scale are added benefits.

We continue along the lines of *Stevens et al*. [2005] and *Yamaguchi and Randall* [2012], and perform simulations based on RF01 of the DYCOMS-II campaign using various domain sizes, grid resolutions and aspect ratios. We start with a setup similar to that of *Kurowski et al*. [2009, 2010] and vary the vertical grid spacing (Δz) between 5 and 35 m, the horizontal grid spacing (Δx and Δy) between 10 and 105 m, and the horizontal extent of the computational domain between 3.5×3.5 and $21\times21\,\mathrm{km}^2$. LES of the STBL is often based on computational grids that are stretched in the vertical direction to achieve a smaller grid spacing near the cloud top—and in some cases near the surface—than elsewhere in the domain. This is a reasonable approach since turbulence in these areas tend to be of smaller scales then turbulence elsewhere in or above the STBL. However, such stretching can be obtained in different ways with potentially different results, and thus we choose to use uniform grids to limit the number of variables in our sensitivity study. The investigated ranges of resolution and domain size are representative of numerous recent LES studies of the STBL, including *de Roode et al*. [2016], *van der Dussen et al*. [2015], *Heinze et al*. [2015], *Jones et al*. [2014], *Connolly et al*. [2013], *Song and Yum* [2012], and *Yamaguchi and Feingold* [2012] using horizontal resolutions between 5 and 120 m, vertical resolutions between 5 and 25 m, and horizontal domain sizes between 3×3 and $16\times16\,\mathrm{km}^2$.

2. Model Description and Setup of Simulations

We use a simplified version of the 3-D nonhydrostatic anelastic Eulerian-semi-Lagrangian (EULAG) model [e.g., *Prusa et al*., 2008], referred to as babyEULAG [*Grabowski*, 2014, 2015]. The code solves for the three velocity components u, v, and w in the x-, y-, and z-directions, the potential temperature θ, the

Table 1. Overview of the Performed Simulations[a]

Name	Δx (m)	Δz (m)	$\Delta x/\Delta z$	L_x (km)	L_z (km)	Cloud Base (m)	Cloud Top (m)	Cloud Thickness (m)
$A_{15,15}$	15	15	1	3.5	1.5	718	830	112
$A_{25,15}$	25	15	1.7	3.5	1.5	722	840	118
$A_{35,15}$	35	15	2.3	3.5	1.5	718	856	138
$A_{45,15}$	45	15	3	3.5	1.5	708	855	147
$A_{55,15}$	55	15	3.7	3.5	1.5	713	851	138
$A_{65,15}$	65	15	4.3	3.4	1.5	695	860	165
$A_{75,15}$	75	15	5	3.5	1.5	693	858	165
$A_{85,15}$	85	15	5.7	3.5	1.5	690	861	171
$A_{95,15}$	95	15	6.3	3.4	1.5	683	859	176
$A_{105,15}$	105	15	7	3.4	1.5	676	858	182
$A_{35,5}$	35	5	7	3.5	1.5	606	862	256
$A_{35,10}$	35	10	3.5	3.5	1.5	676	863	187
$A_{35,20}$	35	20	1.8	3.5	1.5	729	826	97
$A_{35,25}$	35	25	1.4	3.5	1.5	712	808	96
$A_{35,30}$	35	30	1.2	3.5	1.5	702	787	86
$A_{35,35}$	35	35	1	3.5	1.5	689	768	79
$B_{35,35}$	35	35	1	7.0	1.5	684	773	89
$B_{85,15}$	85	15	5.7	7.1	1.5	682	853	171
$C_{35,15}$	35	15	2.3	14.0	1.5	713	850	137
$C_{35,35}$	35	35	1	14.0	1.5	690	780	90
$C_{85,15}$	85	15	5.7	14.2	1.5	682	859	177
$D_{35,35}$	35	35	1	21.0	1.5	691	779	88
$D_{85,15}$	85	15	5.7	21.3	1.5	680	858	178
$A_{10,10}$	10	10	1	3.5	1.5	725	847	123
$A_{20,10}$	20	10	2	3.5	1.5	701	860	160
$A_{70,10}$	70	10	7	3.5	1.5	639	861	222
$A_{105,10}$	105	10	10.5	3.4	1.5	623	858	234
$A_{20,5}$	20	5	4	3.5	1.5	633	867	234
$A_{70,5}$	70	5	14	3.5	1.5	579	856	277

[a]Resolution and domain size as well as mean cloud base, top and thickness averaged over the last 2 h of the performed simulations. We keep $\Delta y = \Delta x$ and $L_y = L_x$.

concentration c of a passive scalar, and for the mixing ratios of water condensate q_c and water vapour q_v. The governing equations are written in the Eulerian form, and as in the EULAG model the nonoscillatory forward-in-time integration is based on the MPDATA [*Smolarkiewicz*, 2006]. We do not apply an explicit SGS model, but rely on the ability of the MPDATA to implicitly account for the effect of the unresolved turbulence on the resolved flow through the truncation terms associated with the algorithm [*Grinstein et al*., 2007; *Grabowski*, 2014, 2015]. Since there was no significant precipitation during DYCOMS-II RF01, we do not include precipitation in our simulations. The amount of condensation/evaporation at each time step is determined by an assumption of no supersaturation (following *Grabowski and Smolarkiewicz* [1990, 2002] and *Grabowski and Jarecka* [2015]). The flow is periodic across the lateral boundaries, while the lower boundary is impermeable with a "partial slip" condition characterized by a specified drag coefficient, and the upper boundary is impermeable with a "free slip" condition.

The study consists of 29 simulations each labeled by a letter denoting the domain size (A, B, C or D) followed by numbers indicating the horizontal and vertical grid intervals in meters. In all simulations we keep $\Delta x = \Delta y$. Domain size A is approximately $3.5\times3.5\times1.5\ \mathrm{km}^3$ (in x-, y-, and z-directions, respectively; L_x, L_y, L_z), B is $7\times7\times1.5\ \mathrm{km}^3$, C is $14\times14\times1.5\ \mathrm{km}^3$, and D is $21\times21\times1.5\ \mathrm{km}^3$. In two main series of simulations we (1) vary the horizontal grid spacing between 15 and 105 m while keeping the vertical grid spacing fixed at 15 m, and (2) vary the vertical grid spacing between 5 and 35 m with the horizontal grid spacing fixed at 35 m. In addition, we perform series of simulations with $\Delta z = 10$ m ($A_{10,10}$, $A_{20,10}$, $A_{35,10}$, $A_{70,10}$, and $A_{105,10}$) and with $\Delta z = 5$ m ($A_{20,5}$, $A_{35,5}$, and $A_{70,5}$). An overview of the simulations is given in Table 1. Initial and ambient conditions are determined by the following profiles of the liquid water potential temperature θ_l, total water mixing ratio q_t, and velocity components (following *Stevens et al*. [2005]):

$$\theta_l = \begin{cases} 289.0\ \mathrm{K} & \text{for } z \le z_i \\ 297.5 + (z - z_i^+)^{1/3}\ \mathrm{K} & \text{for } z \ge z_i^+ \end{cases} \quad (1)$$

$$q_t = \begin{cases} 9.0\,\mathrm{g\,kg^{-1}} & \text{for } z \le z_i \\ 1.5\,\mathrm{g\,kg^{-1}} & \text{for } z \ge z_i^+ \end{cases} \tag{2}$$

$$u = \begin{cases} 6.0\,\mathrm{m\,s^{-1}} & \text{for } z \le z_i \\ 7.0\,\mathrm{m\,s^{-1}} & \text{for } z \ge z_i^+ \end{cases} \tag{3}$$

$$v = \begin{cases} -4.25\,\mathrm{m\,s^{-1}} & \text{for } z \le z_i \\ -5.5\,\mathrm{m\,s^{-1}} & \text{for } z \ge z_i^+ \end{cases} \tag{4}$$

The variables vary linearly between $z_i = 840\,\mathrm{m}$ and $z_i^+ = 875\,\mathrm{m}$. We specify this explicitly to have approximately the same initial profiles regardless of Δz. The initial concentration of the passive scalar is given by:

$$c = \begin{cases} 0 & \text{for } z < z_i^+ \\ 1 & \text{for } z \ge z_i^+ \end{cases} \tag{5}$$

Following *Grabowski* [2015] we apply prescribed fluxes of sensible and latent heat near the surface through

$$h(z) = H_0 \mathrm{e}^{-z/h_d} \tag{6}$$

and

$$q(z) = Q_0 \mathrm{e}^{-z/h_d}. \tag{7}$$

with $H_0 = 15\,\mathrm{W\,m^{-2}}$ and $Q_0 = 115\,\mathrm{W\,m^{-2}}$. The attenuation length h_d is set to 50 m (based on the value used by *Piotrowski et al.* [2009]). Surface fluxes of momentum are applied through

$$\tau_{uw}(z) = -C_d \bar{\rho}^s |\mathbf{u}^s| u^s \mathrm{e}^{-z/h_d} \tag{8}$$

and

$$\tau_{vw}(z) = -C_d \bar{\rho}^s |\mathbf{u}^s| v^s \mathrm{e}^{-z/h_d} \tag{9}$$

where superscript s refers to surface values, $\bar{\rho}$ is the air density in the idealized anelastic base state [see e.g., *Clark and Farley*, 1984], and $|\mathbf{u}| = \sqrt{u^2 + v^2}$ is the wind speed. The drag coefficient C_d is set to 0.001. The vertical divergence of (6)-(9) provides the source of temperature and humidity and the sink of horizontal momentum near the ocean surface.

We apply a longwave radiative flux given by

$$F_{\mathrm{rad}} = \frac{1}{c_p \bar{\rho}} \left(F_0\, \mathrm{e}^{-Q(z,\infty)} + F_1\, \mathrm{e}^{-Q(0,z)} \right) \tag{10}$$

where

$$Q(a,b) = \kappa \int_a^b \bar{\rho} q_c dz. \tag{11}$$

κ, F_0, F_1 are tuning parameters, and c_p is specific heat at constant pressure. It is a simplified version of the radiative flux model used in *Stevens et al.* [2005]. In agreement with *Stevens et al.* [2005] we observe no substantial differences between simulations using the simplified version and simulations using the full version of the model. We use $\kappa = 85\,\mathrm{m^2\,kg^{-1}}$, $F_0 = 70\,\mathrm{W\,m^{-2}}$ and $F_1 = 22\,\mathrm{W\,m^{-2}}$. The vertical divergence of (10) provides cloud-top cooling and cloud-base warming mimicking effects of the longwave radiation. Large-scale subsidence is prescribed as $w_s = -Dz$ with $D = 3.75 \cdot 10^{-6}\,\mathrm{s^{-1}}$, and the large-scale horizontal pressure gradient is applied through the geostrophic wind components of $u_g = 7.0\,\mathrm{m\,s^{-1}}$ and $v_g = -5.5\,\mathrm{m\,s^{-1}}$. The Coriolis parameter is set to $f = 7.3 \cdot 10^{-5}\,\mathrm{s^{-1}}$. All simulations are run for 6 h. For reasons that will become apparent in the discussion of model results, snapshots of model fields are saved every 2 min during the first 2 simulation hours and every 20 min during the last 4 simulation hours.

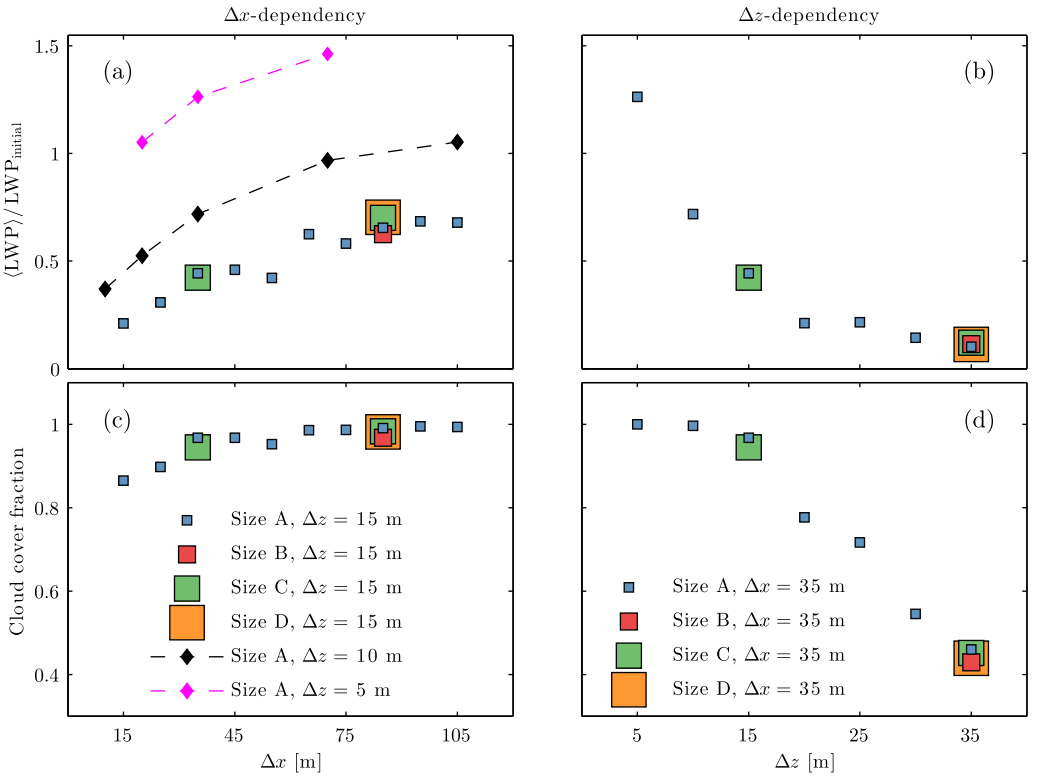

Figure 1. (a and b) Domain-averaged LWP relative to the initial value $LWP_{initial}$ and (c and d) cloud cover fraction as functions of (a and c) Δx and (b and d) Δz. Both quantities are averaged over the period between 240 and 360 min of simulation time. The symbol size increases with domain size.

3. Results

Figure 1 shows the domain-averaged liquid water path $\langle LWP \rangle$ relative to the initial value $LWP_{initial}$ and the cloud cover fraction as functions of $\Delta x = \Delta y$ and Δz. Both quantities are averaged over the period between 240 and 360 min of the simulation time. The cloud cover—defined as the fraction of grid columns with $q_c > 0$ at any height—is initially 1 in all simulations, and $LWP_{initial} \simeq 60\,g\,m^{-2}$. The symbol size reflects the horizontal domain size. $\langle LWP \rangle$ decreases from its initial value making $LWP^* = \langle LWP \rangle / LWP_{initial} < 1$ in all simulations except $A_{20,5}$, $A_{35,5}$, $A_{70,5}$, and $A_{105,10}$. For a fixed vertical grid spacing of $\Delta z = 15$ m, LWP^* increases with increasing Δx (square markers in Figure 1a), while for a fixed horizontal grid spacing of $\Delta x = 35$ m, LWP^* decreases with increasing Δz (square markers in Figure 1b). The cloud cover (square markers in Figures 1c and 1d) follows the general tendency of LWP^*: it increases with increasing Δx and decreases with increasing Δz. In simulations with $\Delta z = 10$ m ($A_{10,10}$, $A_{20,10}$, $A_{35,10}$, $A_{70,10}$, and $A_{105,10}$) and $\Delta z = 5$ m ($A_{20,5}$, $A_{35,5}$, and $A_{70,5}$) the cloud cover fraction (not shown) stays very close to 1 regardless of changes in Δx. LWP^* on the other hand clearly decreases with Δx as indicated by the black ($\Delta z = 10$ m) and purple ($\Delta z = 5$ m) diamond markers in Figure 1a. These additional simulations furthermore show that the Δz-sensitivity regarding LWP^* seen in Figure 1b for $\Delta x = 35$ m also applies for other values of Δx.

Figure 2 shows selected data points from Figure 1 grouped based on the grid aspect ratio. Blue markers represent simulations $A_{10,10}$, $A_{15,15}$, and $A_{35,35}$, red markers $A_{20,10}$, $A_{25,15}$, and $A_{35,20}$, green markers $A_{20,5}$, $A_{35,10}$, and $A_{55,15}$, and orange markers $A_{35,5}$, $A_{70,10}$, and $A_{105,15}$. For all four aspect ratios (1, ∼2, ∼4 and 7) LWP^* decreases with increasing grid spacing (here we use Δx on the horizontal axis, but with $\Delta x/\Delta z$ fixed we could just as well have chosen to use Δz). Overall, the figure shows that grids with high aspect ratios show less sensitivity to the selected grid spacing than grids with aspect ratio close to unity (i.e., the lines become more horizontal with the increasing aspect ratio). This is especially evident in the cloud cover plot. The figure also indicates, that between the opposite effects of increasing Δx and Δz individually, the

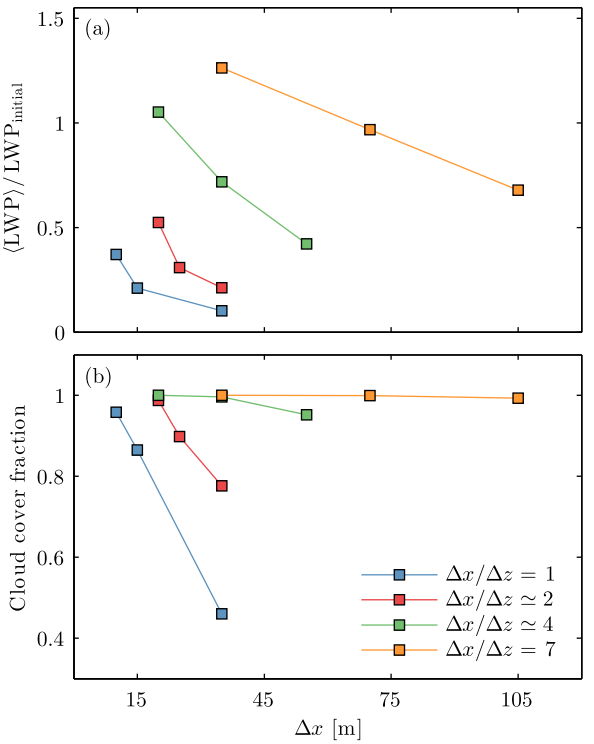

Figure 2. (a) Domain-averaged LWP relative to the initial value $\mathrm{LWP}_{\mathrm{initial}}$ and (b) cloud cover fraction as functions of the grid spacing. We show values averaged over the period between 240 and 360 min in simulations with grid aspect ratios ($\Delta x/\Delta z$) of 1, ~2, ~4, and 7.

Δz-dependency dominates when the grid-lengths are increased simultaneously (in agreement with *Stevens et al.* [2002] and *Matheou and Chung* [2014]).

In the following sections we will report in more detail on the dependence on horizontal grid spacing (section 3.1) and the dependence on vertical grid spacing (section 3.2). We will focus on the two main series of simulations with Δz fixed at 15 m and Δx at 35 m respectively, but will include results from other simulations when relevant. In section 3.3, we investigate the influence of domain size.

3.1. Dependence on the Horizontal Grid Spacing

The observed differences among the performed simulations (Figures 1 and 2) become apparent already during the first 2 h of the simulation time. The temporal evolution of $\langle \mathrm{LWP} \rangle$ from simulations with Δz fixed at 15 m is shown in Figure 3a. The horizontal grid spacing varies from 105 m (dark blue line) to 15 m (dark red line). We observe nearly the same initial sequence in all 10 simulations: a period of slightly increasing $\langle \mathrm{LWP} \rangle$ is followed by a period with clearly decreasing values. The decrease tends to start later and is less significant as Δx is increased. Around the time $t = 40$ min, $\langle \mathrm{LWP} \rangle$ shortly stabilizes, and then continues to decrease in simulations with small Δx, while there is an increase followed by a decrease in simulations with large Δx. At $t \simeq 100$ min the $\langle \mathrm{LWP} \rangle$ reaches a level about which it fluctuates throughout the rest of the simulation period.

We find that the initial decrease in $\langle \mathrm{LWP} \rangle$, starting between $t \simeq 15$ and $t \simeq 30$ min depending on Δx (the smaller Δx the earlier), coincides with increased entrainment which in turn is associated with increased energy of vertical velocity fluctuations at the cloud top [see also *Moeng et al.*, 1996]. Here we define the cloud top/cloud base as the average of the highest/lowest altitude in each grid column at which $q_c > 0$ at a given time step. In the simulations presented here, the cloud base is initially at $z \simeq 615$ m, and the cloud top is at $z \simeq 840$ m. To estimate the entrainment rate, we apply a passive scalar, with the initial concentration of $c = 1$ in the free atmosphere and $c = 0$ in the STBL. The scalar is subjected to advection and large scale subsidence. In Figure 3b, we show the temporal derivative of c integrated between the surface and the local cloud top:

$$\dot{C} = \frac{\partial}{\partial t} \left\langle \int_0^{z_{\mathrm{top}}} c \, dz \right\rangle \tag{12}$$

as a function of time. As before, the angular bracket denotes the horizontal domain average. Finally, in Figure 3c, we show the vertical velocity variance $\langle w'w' \rangle$ at the cloud top as a function of time. We define $w' = w - \langle w \rangle$. Distinct peaks at, say, $t = 20$ and $t = 42$ min in simulation $\mathrm{A}_{15,15}$, coincide with the entrainment rate estimated by $\dot{C}$ approaching its maximum, and the beginning of a decrease in $\langle \mathrm{LWP} \rangle$.

The peak values of $\langle w'w' \rangle$ at the cloud top increase with decreasing Δx, leading to more entrainment and lower $\langle \mathrm{LWP} \rangle$. The temperature inversion at the top of the STBL limits the size of turbulent eddies there. These eddies are to a larger extent resolved with a smaller horizontal grid spacing; hence the higher values of $\langle w'w' \rangle$. To illustrate this, we show velocity fluctuations in segments of vertical cross sections from simulations $\mathrm{A}_{105,15}$ and $\mathrm{A}_{15,15}$ in Figure 4. The cross sections are aligned with the instantaneous mean wind

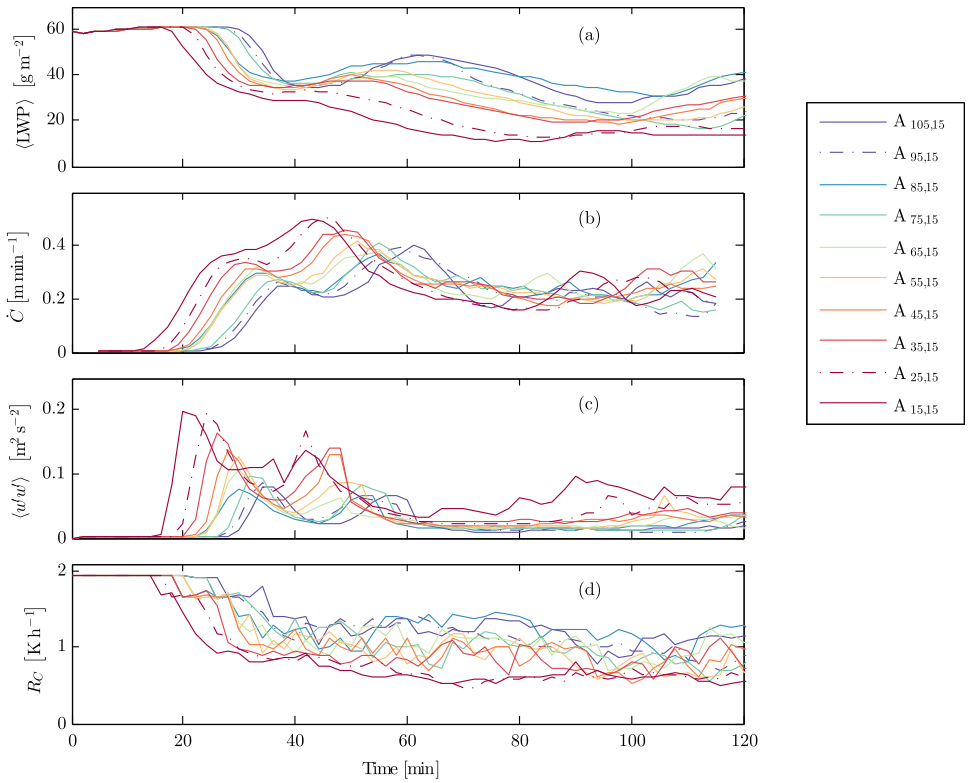

Figure 3. Time series of (a) domain-averaged LWP, (b) temporal derivative of passive scalar concentration integrated across the STBL, (c) variance of vertical velocity at cloud top, and (d) radiative cooling across the cloud top for simulations of varying Δx.

direction across the STBL, and the arrows indicate the direction and magnitude of in-plane velocity fluctuations. In both panels of Figure 4, we interpolated the original velocity fields to points separated by 15 m in the direction of the mean wind. The horizontal axis denotes the distance from $(x, y) = (0, L_y)$, and the two red lines indicate local cloud base and cloud top. In simulation $A_{105,15}$ we use values from $t = 36$ min, and in $A_{15,15}$ from $t = 20$ min, corresponding to the times of the initial peaks in $\langle w'w' \rangle$. The shown segments are representative of the general situation in the two simulations at these times. Both simulations are dominated by turbulent eddies centred in the upper part of the cloud layer. While they often reach all the way to the cloud base or below and tend to be anisotropic in $A_{105,15}$ (width-to-height ratio greater than 1), they typically only occupy the upper half of the cloud layer in $A_{15,15}$ and have a width-to-height ratio close to 1. We find that the large coarse-resolution eddies lead to the highest total cloud-top turbulent kinetic energy (TKE), while the smaller high-resolution eddies lead to the highest vertical component of the TKE at the cloud top. The correlation between cloud-top $\langle w'w' \rangle$, entrainment rate, and $\langle \text{LWP} \rangle$ becomes less pronounced after ∼60 min of simulation time. This is likely because convective eddies spanning the STBL generated by a combination of surface heating and cloud-top cooling also begin to play a role in the entrainment process.

Decreased $\langle \text{LWP} \rangle$ leads to decreased radiative cooling, and thereby less production of vertical TKE near the cloud top. The cloud-top radiative cooling R_C, calculated as the mean vertical divergence of F_{rad} between the middle of the cloud layer, i.e., halfway between the cloud base and the cloud top, and the first grid point above the cloud top, is shown in Figure 3d. Less vertical TKE leads to less entrainment and subsequent stabilization of $\langle \text{LWP} \rangle$. In simulation $A_{15,15}$ this happens at $t \simeq 80$ min and in $A_{105,15}$ at $t \simeq 110$ min.

As noted by *Stevens et al.* [2005], decreased radiative cooling can also lead to a decoupling, that is, a situation where an initially well-mixed STBL evolves toward a two-layer structure despite being strongly forced—in this case by a large-scale horizontal pressure gradient corresponding to a geostrophic wind of 8.9 m s^{-1} and surface sensible and latent heat fluxes of 15 and 115 W m^{-2} [*Stevens*, 2000]. Analyzing the 2 last hours of the simulation time, we see some evidence of decoupling in the performed simulations. Figure

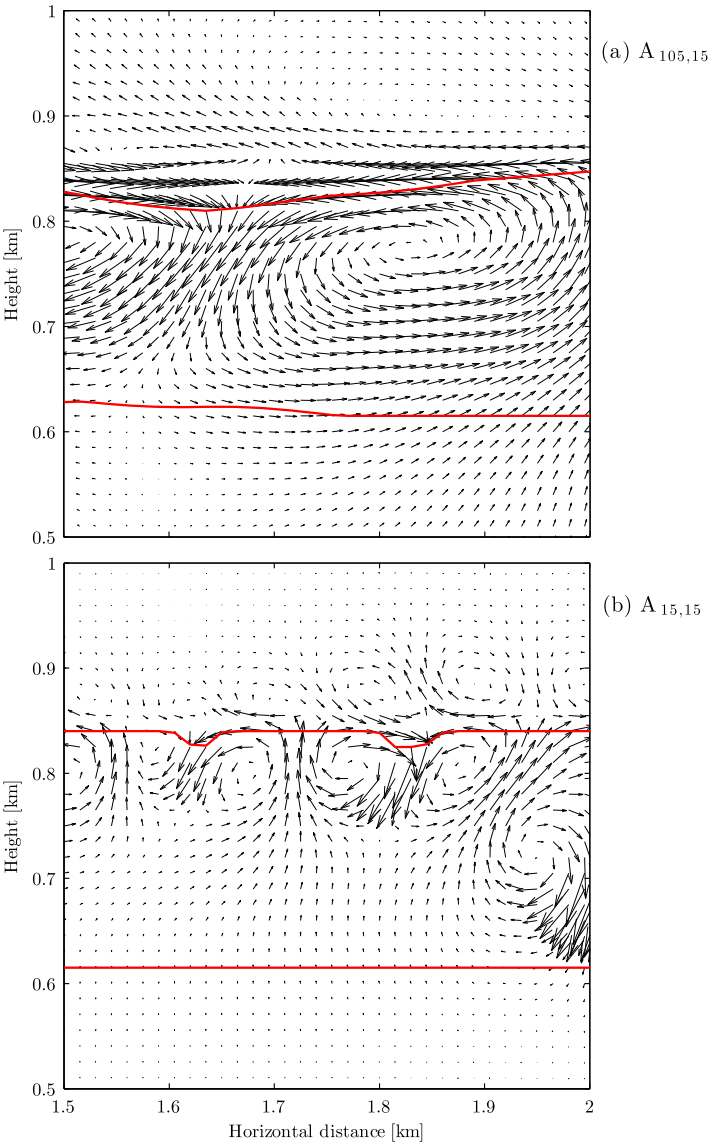

Figure 4. Segments of vertical cross sections showing in-plane velocity fluctuations from (a) simulation $A_{105,15}$ and (b) simulation $A_{15,15}$. Red lines indicate local cloud base and top.

5 shows vertical profiles of domain-averaged passive scalar concentration averaged over this period. In simulations with Δz=15 m (Figure 5a) increasing Δx and thereby $\langle$LWP$\rangle$ (as seen in Figure 1) generally leads to better mixed profiles. The same is seen for the wind speed—also averaged over the domain and over the final 2 h—shown in Figure 6 in the same format as Figure 5. Increasing Δx tends to decrease wind shear in the middle region of the STBL (100 m $\leq z \leq$ 500 m approximately); an effect very similar to that of slightly increasing the surface heat flux [*Pedersen et al*., 2014]. Regarding both scalar concentration and wind speed we also see the tendency of better mixed profiles with increasing Δx when using Δz= 10 m, but not with Δz=5 m; the horizontally averaged passive scalar concentration is nearly constant with height within the STBL in both $A_{20,5}$, $A_{35,5}$, and $A_{70,5}$ (dark-red dashed, solid, and dash-dot lines in Figure 5b), but decreases throughout the STBL with increasing Δx. The wind speed shows no systematic dependence on Δx when Δz=5 m. Altitudes of cloud top and cloud base averaged over the period between t = 240 and t = 360 are marked by long and short horizontal lines along the vertical axes in Figure 5. Values from simulations not included in Figure 5 can be found in Table 1 which also provides the cloud thickness. Increasing Δx generally leads to a lower cloud base and a higher cloud top, and hence a thicker cloud.

Figure 7 shows vertical profiles of the second and third moments of vertical velocity averaged between 240 and 360 min of simulation time. The crosses represent estimates derived from in situ measurements (taken from *Stevens et al*. [2005, Figure 5]). Coarsening the horizontal resolution in simulations with Δz=15 m (Figures 7a and 7b) has little effect on $\langle w'w' \rangle$, but generally tends to reduce $\langle w'w'w' \rangle$, that is, to make the STBL less updraft-dominated leading to a better agreement with the measurements in the upper half of the STBL (above 400 m) but worse near the surface (below 200 m). None of the simulations with Δz fixed at 15 m, however, reproduce the clearly downdraft-dominated cloud layer indicated by the negative values of $\langle w'w'w' \rangle$ derived from measurements. This was also the case with simulations reported in *Kurowski et al*. [2009], see Figure 2 therein. With Δz=5 m (dark-red dashed, solid, and dash-dot lines in Figures 7c and 7d) the cloud-layer $\langle w'w'w' \rangle$ is negative in all simulations—slightly more so in $A_{70,5}$ and $A_{35,5}$ than in $A_{20,5}$. Regarding $\langle w'w' \rangle$, we see little difference between $A_{35,5}$ and $A_{20,5}$, while $A_{70,5}$ gives lower values at all heights. Finally we note that $A_{105,10}$ (dashed green line in Figures 7c and 7d) is the only simulation with

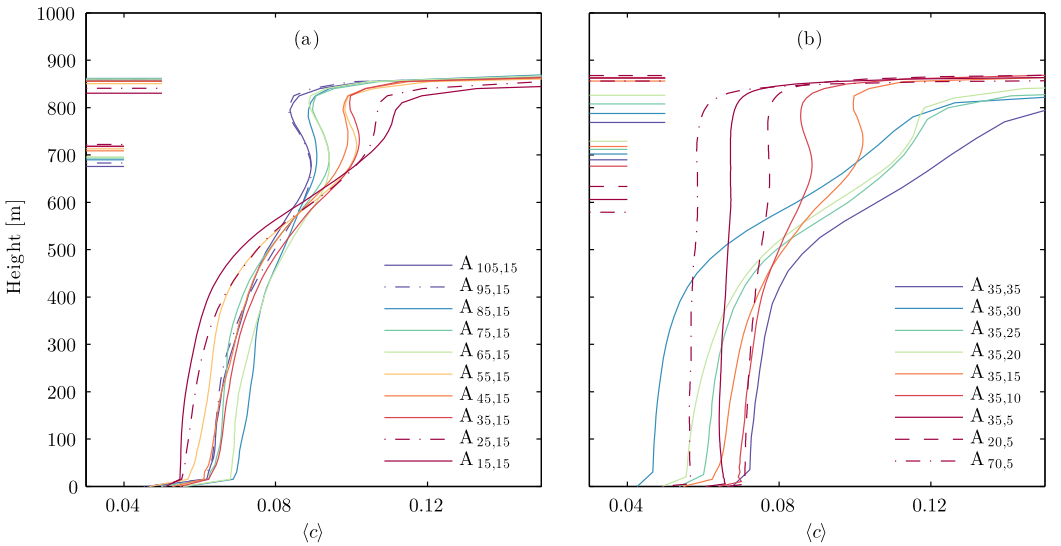

Figure 5. Vertical profiles of passive scalar concentration averaged over the period between 240 and 360 min of simulation time; (a) simulations of varying Δx and (b) simulations of varying Δz (solid lines) and Δx (dark red lines). Short/long horizontal lines indicate cloud base/top.

Δz=10 m to produce negative values of $\langle w'w'w' \rangle$ in the cloud layer. The shape of the corresponding $\langle w'w' \rangle$ profile resembles that of the profiles from simulations with Δz=5 m, but the absolute $\langle w'w' \rangle$ values are closer to those from simulations with Δz=15 m.

In the following we present a spectral analysis which will allow us to: (1) asses the fidelity of the model in terms of its ability to produce an inertial subrange, (2) obtain characteristics of the simulated turbulence (e.g. level of isotropy) at different scales and at different vertical levels, and (3) estimate whether the applied computational domains are sufficiently large.

Figures 8a and 8b show the spectral energy density of vertical velocity E_w (solid lines) from simulations with different Δx. Following *Peltier et al.* [1996] we define

$$E_w(\kappa) = \frac{2\pi\kappa F_w F_w^*}{\Delta\kappa_x \Delta\kappa_y} \tag{13}$$

where * denotes the complex conjugate, $\kappa = \left(\kappa_x^2 + \kappa_y^2\right)^{1/2}$ is the magnitude of the wavenumber vector and $F_w(\kappa_x, \kappa_y) = \mathrm{FFT2}\{w(x,y)\}$. Here FFT2 denotes fast fourier transform (FFT) first along the x-direction for all y-values, followed by FFT of the result along the y-direction for all κ_x-values. The FFT computes

$$X(j) = \frac{1}{N}\sum_{k=1}^{N} Y(k) e^{\frac{2\pi i}{N}(j-1)(k-1)} \text{ for } j = 1, 2, \ldots, N \tag{14}$$

where N is the number of data points in Y.

The components of the wavenumber vector are defined by

$$\kappa_x = \frac{2\pi n_x}{L_x} \text{ for } n_x = 1, 2, \ldots, \frac{L_x}{\Delta x} \tag{15}$$

and

$$\kappa_y = \frac{2\pi n_y}{L_y} \text{ for } n_y = 1, 2, \ldots, \frac{L_y}{\Delta y} \tag{16}$$

We plot E_w as a function of the wavelength defined by $\lambda = 2\pi/\kappa$. The blue, red, green and orange lines are from simulations $D_{85,15}$, $A_{85,15}$, $A_{45,15}$ and $A_{15,15}$ and represent averages over bins of λ-values and over the last hour of the simulation. The blue dash-dot lines represent the spectral energy density of potential temperature E_θ and will be dicussed with respect to domain size in section 3.3. Figures 8a and 8c show spectra

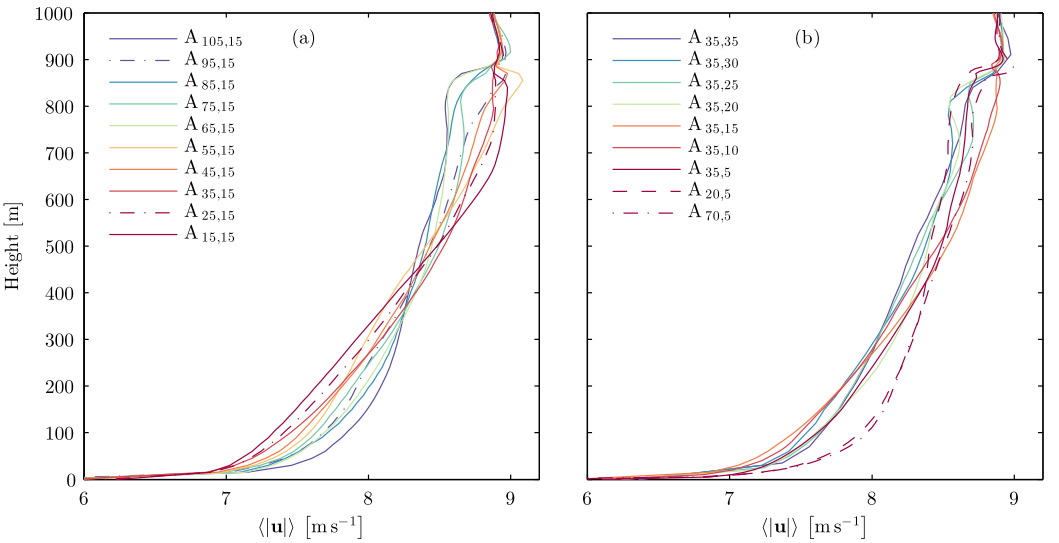

Figure 6. Same as Figure 5 but for wind speed.

from the middle of the subcloud layer (defined as the layer between the surface and the cloud base), and Figures 8b and 8d show spectra from near the cloud top. The exact altitudes are given in the figure.

In the subcloud layer, the simulation with the highest resolution ($A_{15,15}$) show the expected $E_w \propto \kappa^{-5/3}$ scaling (black dashed line) over a relatively wide range of wavelengths (approximately from 1000 m down to 200 m). However, we see less evidence of an inertial subrange as Δx is increased, and the spectra indicate that the model is too dissipative. At the cloud top the vicinity of the capping inversion limits the size of the

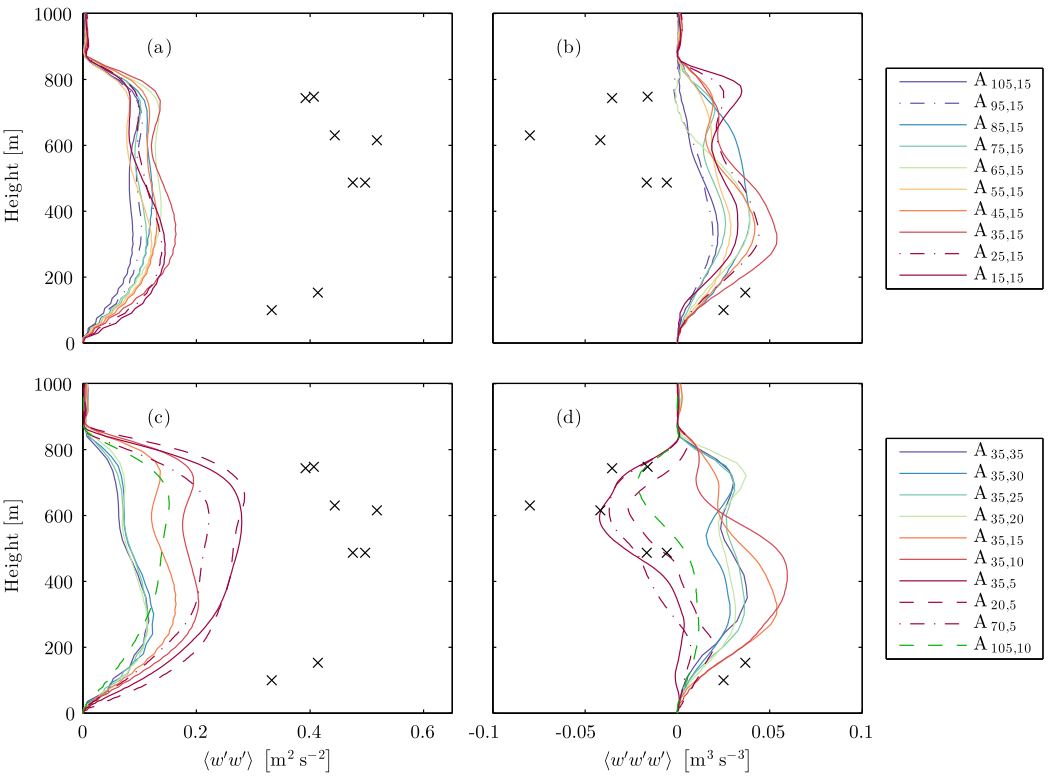

Figure 7. Same as Figure 5 but for (a and c) $\langle w'w' \rangle$ and (b and d) $\langle w'w'w' \rangle$. Crosses are estimates derived from in situ measurements (taken from *Stevens et al.* [2005]).

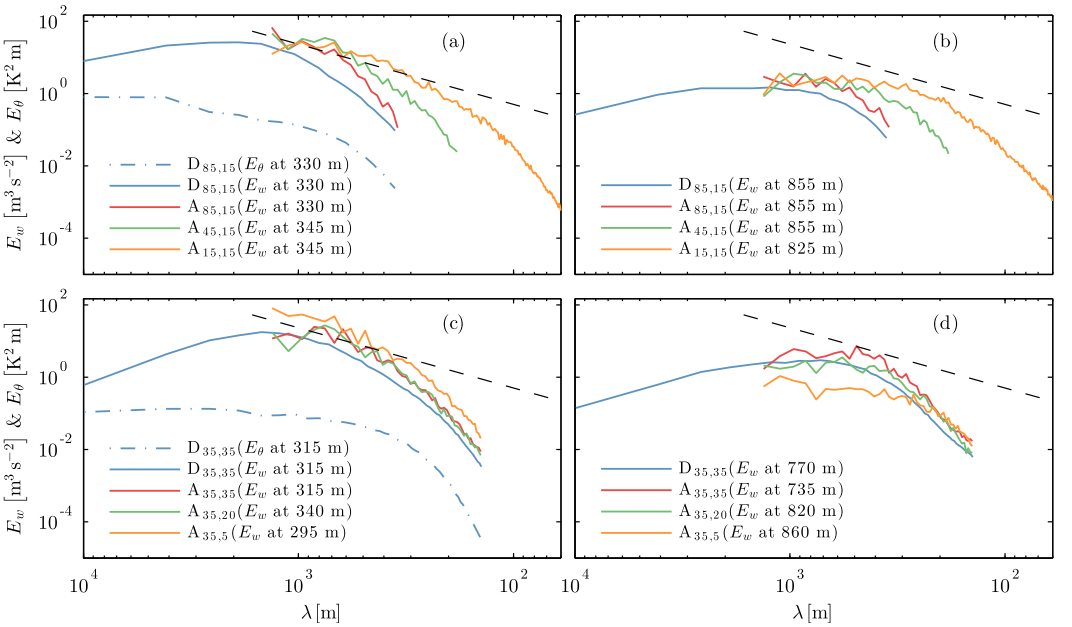

Figure 8. Spectral energy density of vertical velocity E_w (solid lines) and potential temperature E_θ (dash-dot lines) from simulations with (a and b) different Δx, (c and d) different Δz and different domain sizes. Solid and dash-dot lines represent averages over bins of λ-values and over the last hour of the simulation period; (a and c) from the middle of the subcloud layer, and (b and d) from near the cloud top. The black dashed line represents $E_w \propto \kappa^{-5/3}$.

turbulent eddies, and the spectra show short or no inertial subranges. This is in agreement with *Yamaguchi and Randall* [2012] who show that the longest wavelength of the inertial subrange decreases with increasing height. The spectra from the middle of the subcloud layer are comparable to those presented in *Bryan et al*. [2003, Figure 10], *Piotrowski et al*. [2009, Figure 16], and *Yamaguchi and Feingold* [2012, Figure 2], but clearly inferior when compared to those obtained using a pseudo-spectral model (e.g., as shown by *Sullivan and Patton* [2011, Figure 7]). Averaging over all the performed simulations we find that the inertial subrange extends down to $\lambda \simeq 8\Delta x$ (see supporting information).

The spectral energy density of horizontal and vertical velocity components E_u, E_v, and E_w are compared in Figure 9 using blue, red, and green lines, respectively. Panels (a) and (b) show spectra from simulation A$_{15,15}$ from the subcloud layer and the cloud top. In the subcloud layer, the three spectra nearly overlap at all wavelengths indicating isotropic turbulence. Near the cloud top, on the other hand, E_w is significantly smaller than E_u and E_v at scales larger than ~300 m. The latter indicates that the turbulence is anisotropic at these scales. Increasing the horizontal grid spacing to 35 m (panels c and d), makes the observed anisotropy even more pronounced.

3.2. Dependence on the Vertical Grid Spacing

As shown in Figure 1d, decreasing Δz tends to increase cloud cover and, especially for $\Delta z \leq 20$ m, also $\langle$LWP$\rangle$ as seen in Figure 1b. We find this to be related to the strength of the capping inversion. Refining the vertical resolution allows stronger vertical gradients which strengthens the inversion and inhibits entrainment. This is illustrated in Figure 10 showing $\langle$LWP$\rangle$, entrainment rate based on changes in integrated passive scalar concentration, maximum vertical gradient of horizontally averaged density potential temperature $\Gamma_{\max}$, and radiative cooling across the cloud top for simulations with fixed $\Delta x = 35$ m, and Δz varying between 5 m (dark red line) and 35 m (dark blue line). For this subset of simulations, the most significant changes in $\langle$LWP$\rangle$ happen within the first 2 h. Simulation A$_{35,5}$ stands out as it is the only simulation with $\Delta x = 35$ m in which $\langle$LWP$\rangle$ continues to increase throughout the simulation period (from $t = 80$ min onward).

Furthermore, averaging over the last 2 h of the simulation period, profiles of the passive scalar concentration in Figure 5b indicate that A$_{35,5}$ is the simulation with the best mixed STBL. A well mixed boundary layer

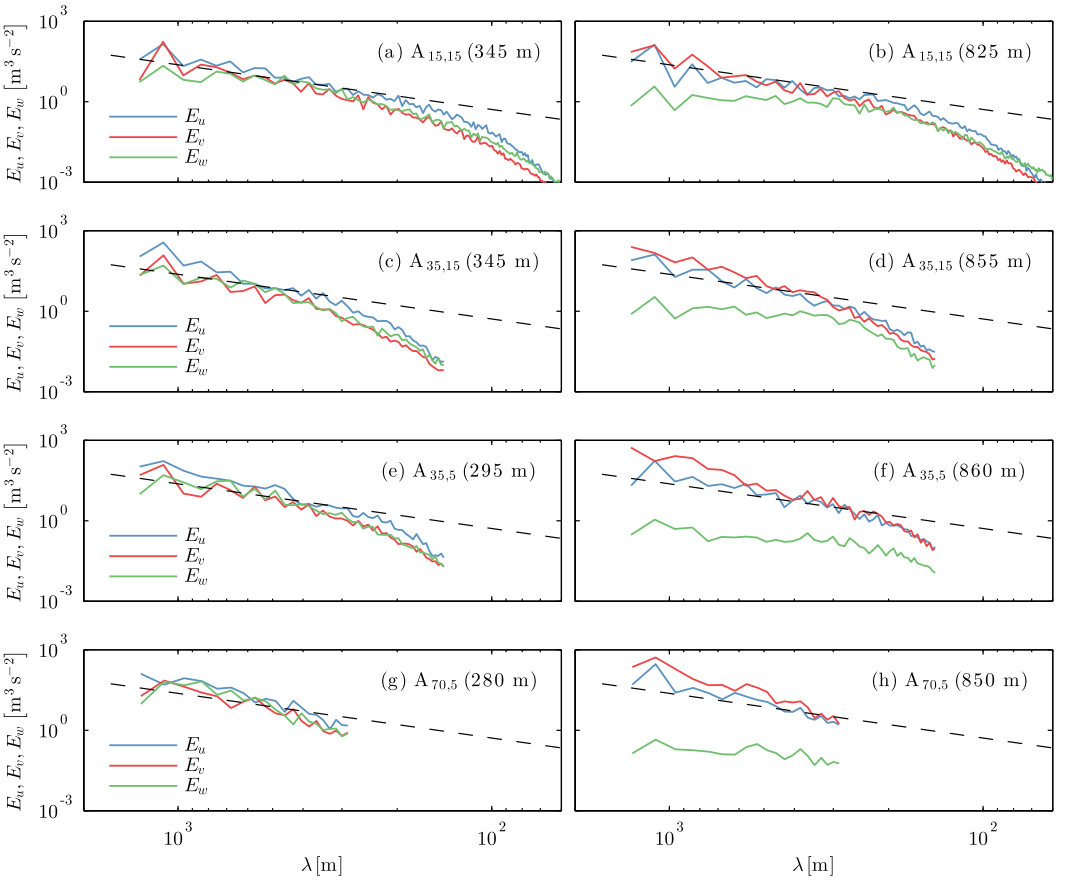

Figure 9. Spectral energy density of horizontal and vertical velocities (E_u, E_v, and E_w) represented by blue, red and green lines from simulation (a and b) $A_{15,15}$, (c and d) $A_{35,15}$, (e and f) $A_{35,5}$, and (g and h) $A_{70,5}$; (a, c, e, and g) from the middle of the subcloud layer, and (b, d, f, and h) from near the cloud top. The black dashed line represents $\kappa^{-5/3}$ scaling.

is in agreement with the experimental profiles of q_t and θ_l [cf. *Stevens et al.*, 2003, Figure 2]. Generally, with increasing Δz (and thereby decreasing $\langle \mathrm{LWP} \rangle$ as seen in Figure 1), a smaller fraction of entrained passive scalar is transported to the surface layer; this is most clearly seen for $\Delta z \leq 20$ m. The ratios between the mean passive scalar concentration at $z \simeq 700$ m and the concentration at $z \simeq 100$ m are 1.7, 2.2, 1.8, 2.0, 1.5, 1.3, and 1.0 for $A_{35,35}$, $A_{35,30}$, $A_{35,25}$, $A_{35,20}$, $A_{35,15}$, $A_{35,10}$, and $A_{35,5}$. The effect on the wind speed profiles shown in Figure 6b is less pronounced.

The profiles of $\langle w'w' \rangle$ averaged over the last 2 h are shown in Figure 7c. Decreasing Δz generally leads to higher values and moves the maximum of $\langle w'w' \rangle$ from the subcloud layer to the cloud layer, bringing the simulated profiles closer to the observations. We argue that this is in part because decreasing Δz leads to higher $\langle \mathrm{LWP} \rangle$, stronger radiative cooling (as shown in Figure 10) and thereby a more turbulent STBL (especially near the top), but also in part because higher resolution in itself means that more turbulent eddies are resolved and hence the higher values of $\langle w'w' \rangle$. Furthermore, refining the vertical resolution changes the third moment (Figure 7d) from positive to negative above 400 m. Thus the cloud layer changes from being updraft-dominated to downdraft-dominated, in better agreement with the observations. Simulation $A_{35,5}$ stands out in this respect together with $A_{20,5}$, $A_{70,5}$, and $A_{105,10}$. We also note that while the cloud thickness generally increases with decreasing Δz (see Table 1), simulation $A_{35,5}$ is the only one with $\Delta x = 35$ m in which the cloud thickness increases during the simulation period.

Finally, the spectral energy density of vertical velocity shown in Figure 8 exhibits less dependency on vertical resolution (Figures 8c and 8d) than on horizontal resolution (Figures 8a and 8b). However, near the cloud top, we do see a reduction in E_w at scales larger than ~300 m as Δz is reduced to 5 m. Figures 9e and 9f show that the turbulence in the subcloud layer of simulation $A_{35,5}$ is isotropic, while the cloud-top

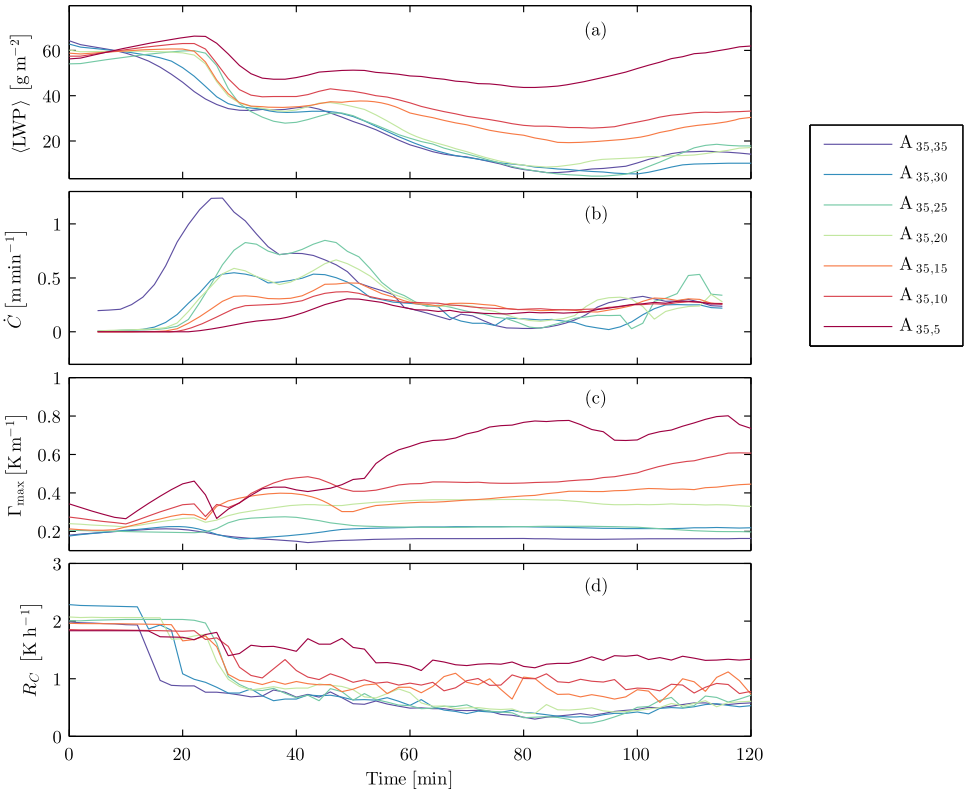

Figure 10. Time series of (a) domain-averaged LWP, (b) temporal derivative of passive scalar concentration integrated across the STBL, (c) maximum vertical gradient of density potential temperature, and (d) radiative cooling across the cloud top for simulations of varying Δz.

turbulence is clearly anisotropic—more so than in $A_{15,15}$, and $A_{35,15}$ (Figures 9b and 9d), and at all scales. Increasing Δx to 70 m while keeping $\Delta z = 5$ m (Figures 9g and 9h) adds further to the anisotropy of the cloud-top turbulence by slightly reducing E_w, cf. the results presented in the previous section 3.1.

3.3. Dependence on the Domain Size

As shown in Figure 1, domain-averaged cloud cover and LWP* do not indicate any significant dependence on the horizontal extent of the computational domain in the range between 3.5×3.5 and 21×21 km^2 studied here. Neither does visual inspection of patterns of updrafts, downdrafts, and cloud cover reveal any clear domain-size sensitivity. We do, however, detect larger coherent structures as the domain size is increased. In Figure 11, we show horizontal cross sections of vertical velocity in the middle of the subcloud layer and in the middle of the cloud layer from simulations $C_{35,15}$ and $A_{35,15}$ (a and b), $C_{35,35}$ and $A_{35,35}$ (c and d), and $C_{85,15}$ and $A_{85,15}$ (e and f). The exact altitudes of the cross sections are given in the figure. Black/red lines mark updrafts/downdrafts with $|w| \geq 0.1$ m s^{-1} and the increment between contours is 0.6 m s^{-1}. The background color in Figures 11b, 11d, and 11f indicates LWP. While the shown cross sections are single snapshots after 360 min of simulation time, the following observations and analysis are based on series of such snapshots captured every 20 min between 240 and 360 min of simulation time.

At a glance, the appearance of the small-domain cross sections do not differ significantly from the corresponding big-domain cross sections. There are however notable differences concerning the size of the largest coherent updrafts. As a measure of the updraft size, we calculate:

$$I = \left(l_x^2 + l_y^2 \right)^{1/2} \tag{17}$$

for each area with $w \geq 0.1$ m s^{-1} in each cross section. Here l_x and l_y denote the dimensions in the x- and y-directions of such an area. An updraft extending across one of the periodic boundaries is taken as one large updraft and not as two smaller updrafts. In each cross section we identify the largest updraft in terms of I and then average over $240 \leq t \leq 360$ min to get $\bar{I}_{\max}$ at a given height. As an example, we have highlighted

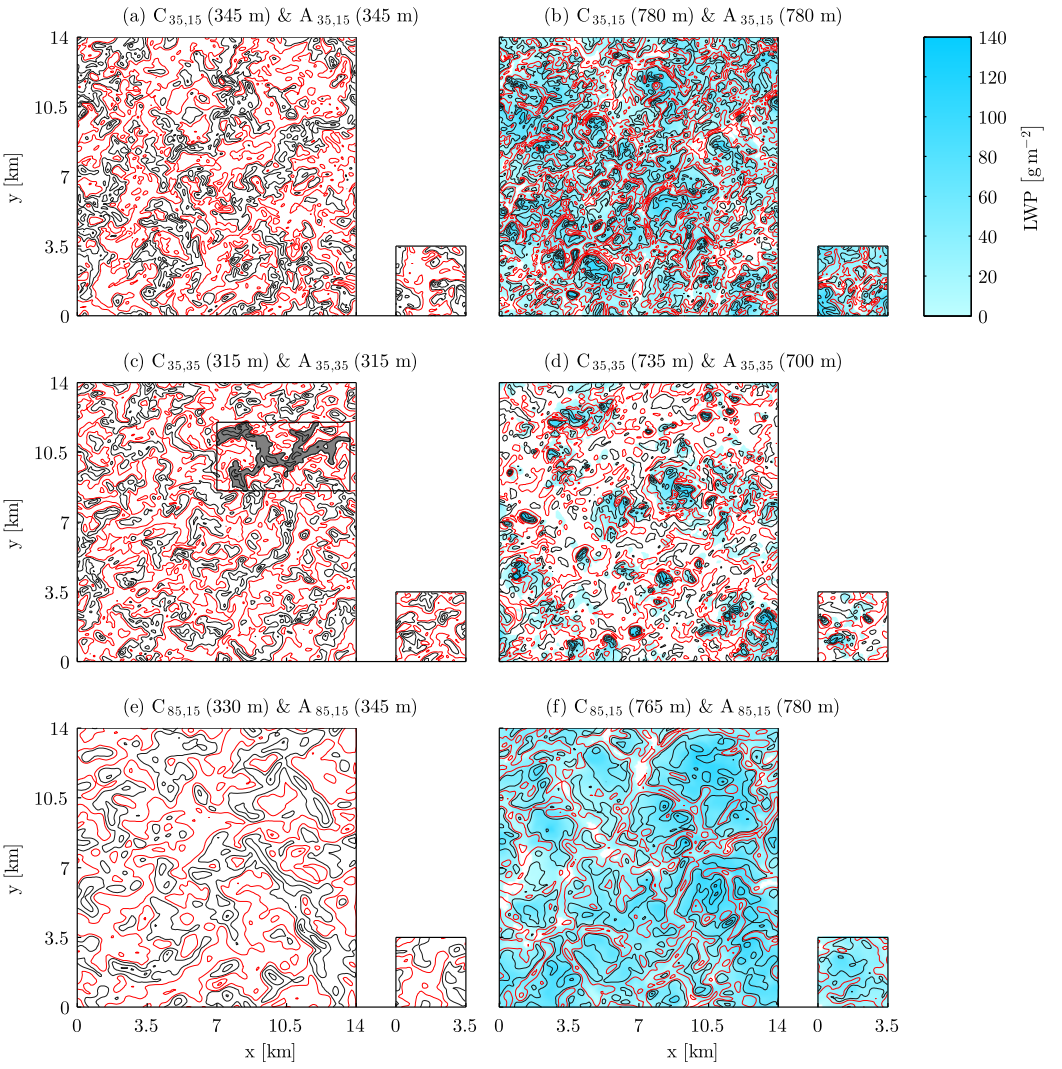

Figure 11. Horizontal cross sections from simulations (a and b) $C_{35,15}$ and $A_{35,15}$, (c and d) $C_{35,35}$ and $A_{35,35}$, and (e and f) $C_{85,15}$ and $A_{85,15}$ showing vertical velocity (contours) and LWP (white-to-blue background color in Figures 11b, 11d, and 11f). Black/red contours mark updrafts/downdrafts with $|w| \geq 0.1\ \mathrm{m\,s^{-1}}$. Values in Figures 11a, 11c, and 11e are from the middle of the subcloud layer and values in Figures 11b, 11d, and 11f are from the middle of the cloud layer. The rectangle in the upper right corner of Figure 11c indicates the position and size of the largest updraft in that cross section highlighted by the grey color.

the largest updraft at $z = 315$ m and $t = 360$ min in simulation $C_{35,35}$, in Figure 11c, and placed a rectangle of side lengths l_x and l_y around it.

In Table 2 we provide values of $\bar{l}_{\mathrm{max}}$ from simulations $A_{35,15}$, $C_{35,15}$, $A_{35,35}$, $B_{35,35}$, $C_{35,35}$, $D_{35,35}$, $A_{85,15}$, $B_{85,15}$, $C_{85,15}$, and $D_{85,15}$. For all three resolutions and for all domain sizes, the values from the subcloud layer are larger than values from the cloud layer, and in simulations with domain sizes B, C, and D, the size of the largest updrafts generally exceeds the horizontal extent of domain A. This, however, does not seem to significantly affect cloud cover or $\langle \mathrm{LWP} \rangle$. The relatively small differences in terms of $\bar{l}_{\mathrm{max}}$ in both the subcloud layer and cloud layer between $C_{35,35}$ and $D_{35,35}$, and $C_{85,15}$ and $D_{85,15}$ respectively, indicate nearly converged solutions with respect to the domain size.

The spectral energy density of vertical velocity in the middle of the subcloud layer (Figures 8a and 8c) exhibits a peak at $\lambda \simeq 1$ km, that is, at a scale smaller than the horizontal extent of even the smallest domains considered here. However, as pointed out by *de Roode et al.* [2004], other fields, such as the potential temperature, may be dominated by fluctuations at larger scales and should be taken into account in a

Table 2. $\bar{l}_{max}$ in Subcloud and Cloud Layers[a]

Name	$\bar{l}_{max}$ in Subcloud Layer (km)	$\bar{l}_{max}$ in Cloud Layer (km)	$L_x \times L_y \times L_z$ (km^3)
$A_{35,15}$	4.3 (0.2)	2.9 (0.5)	3.5×3.5×1.5
$C_{35,15}$	12.3 (3.1)	4.4 (0.7)	14×14×1.5
$A_{35,35}$	3.6 (1.0)	2.0 (0.4)	3.5×3.5×1.5
$B_{35,35}$	5.9 (2.2)	2.7 (0.3)	7×7×1.5
$C_{35,35}$	7.4 (0.9)	3.5 (0.6)	14×14×1.5
$D_{35,35}$	8.1 (2.2)	3.3 (0.5)	21×21×1.5
$A_{85,15}$	3.9 (0.7)	3.2 (0.8)	3.5×3.5×1.5
$B_{85,15}$	8.9 (2.7)	4.1 (0.8)	7×7×1.5
$C_{85,15}$	12.9 (3.5)	6.4 (0.6)	14×14×1.5
$D_{85,15}$	13.9 (3.3)	6.5 (0.9)	21×21×1.5

[a] $\bar{l}_{max}$ calculated in the subcloud layer and in the cloud layer for simulations with varying resolution and domain size. Standard deviations with respect to the time-averaging are written in parentheses after the mean values.

full analysis of whether a given domain is large enough. Spectral energy densities of θ from simulations $D_{85,15}$ and $D_{35,35}$ are shown in Figures 8a and 8c, and the lack of clear spectral peaks indicates that a domain larger than 21×21 km^2 in the horizontal directions may be necessary for accurate simulation of the temperature fluctuations in the case studied here.

4. Discussion and Concluding Remarks

Increasing Δx while keeping Δz fixed generally leads to higher $\langle$LWP$\rangle$ and cloud cover. Increasing Δz while keeping Δx fixed has the opposite effect. This is in agreement with findings shown in Appendix B of *Yamaguchi and Randall* [2012] and in *Cheng et al.* [2010], and regarding the Δz-dependency also with *Kurowski et al.* [2009] and *Stevens et al.* [2005]. The study of *Yamaguchi and Randall* [2012] is based on simulations with higher resolutions than in the present study, while the one of *Cheng et al.* [2010] is based on simulations with coarser resolutions. The results of *Yamaguchi and Randall* [2012] show signs of convergence with respect to resolution, but simulations with grid intervals less than 5 m in the horizontal and 2.5 m in the vertical are needed to verify this. Individually decreasing Δx to 10 m and Δz to 5 m, as is done in the present study, does not indicate convergence. In contrast, *Stevens et al.* [2005] find that changing grid spacing from 35×35×5 m^3 to 20×20×5 m^3 has no significant impact on the flow statistics. We find such a change in resolution to have only little or no impact on cloud cover and profiles of variance and skewness of the vertical velocity, but a significant impact on the domain-averaged liquid water path. It is not clear to which statistics *Stevens et al.* [2005] refer, but we find it likely that the reported lack of Δx-dependency is due to the stochastic nature of LES; as we show, simulations are sensitive to what happens in the early stages, and repeating the simulation with $\Delta x = \Delta y = 20$ m might lead to another result. As an example, we note that in the present study decreasing Δx from 55 to 45 m increases LWP* and cloud cover (see Figure 1). Had this been our only result, we would have reached a conclusion opposite to what we actually find. Due to the relatively large number of simulations included in the study, we are quite confident about our conclusions. Ideally, however, each simulation should be repeated several times.

We show that fine horizontal resolution facilitates formation of small-scale turbulence near the cloud top early in the simulations (particularly for $t < 1$h). This enhances entrainment and reduces $\langle$LWP$\rangle$. Fine vertical resolution strengthens the capping inversion during the first 2 h of simulation, which inhibits entrainment and leads to less reduced or even increased $\langle$LWP$\rangle$. In the specific case studied here (DYCOMS-II RF01), where the measurements indicate a cloud cover above 99% and a constant or perhaps increasing cloud thickness, we find that simulations with a high grid aspect ratio (achieved by using either coarse horizontal or fine vertical resolution) give the best agreement with observations—at least with respect to these two key parameters of stratocumulus clouds, and to some extent also for the profiles of second and third moments of the vertical velocity. In simulation $A_{35,5}$ we see increasing cloud thickness and a nearly constant cloud cover fraction of ∼1 [see also *Kurowski et al.*, 2009], while in $A_{15,15}$, with nearly twice as many grid points, the cloud thickness decreases and the cloud cover fraction is reduced to ∼0.85 after 6 h. Moreover, in simulation $A_{105,15}$—applying only a little more than 1/50 of the grid points used in $A_{15,15}$—the cloud cover remains close to 1 in agreement with the measurements.

To understand why simulations with anisotropic grids, relatively fast in terms of computation time, perform better than the simulation with the isotropic grid, we need to look at the dynamics of turbulent transport across the inversion capping the STBL—the mechanism responsible for entrainment of free tropospheric air into the boundary layer. We present two explanations: First, the thickness of the inversion is typically of the order of 10 m (e.g., see the experimental data from DYCOMS-II in *Haman et al*. [2007] and from POST in *Gerber et al*. [2013]), and only simulations with a vertical grid spacing of a few meters or less can be expected to capture its basic properties, including strong local wind shear and temperature gradients. Thus, with limited computational resources, we find an anisotropic distribution of grid points, resulting in higher vertical than horizontal resolution, to be more desirable than an isotropic distribution with a comparable number of grid points. Second, as indicated by the high-resolution measurements of *Katzwinkel et al*. [2012] and I. Jen-La Plante et al. (Physics of Stratocumulus Top (POST): Turbulence characteristics, submitted to *Atmospheric Chemistry and Physics Discussions*, doi:10.5194/acp-2015-950, 2016), the inversion layer is very stably stratified yet turbulent. It is also well documented that turbulence in stably stratified fluids is highly anisotropic (see the seminal paper of *Lindborg* [2006] and references therein). As discussed e.g., by *Khani and Waite* [2014], the Ozmidov scale $L_O=(\epsilon/N^3)^{1/2}$ (where ϵ is the TKE dissipation rate and N is the buoyancy frequency) divides the inertial range into wavelengths larger than L_O featuring anisotropic turbulence, and wavelengths less than L_O characterized by isotropic turbulence. Recent experimental data from POST (Jen-La Plante et al., submitted manuscript, 2016) show values of the Ozmidov scale in the turbulent inversion ranging between 0.2 and 1.7 m with a typical value of $\sim$0.4 m. Thus, we can assume that cloud-top turbulence at scales typically resolved in LES and relevant for entrainment (i.e., between $\sim$0.5 and $\sim$60 m according to *de Lozar and Mellado* [2013]) is anisotropic; assuming the cloud-top SGS turbulence to be isotropic in LES/ILES of the STBL will in many cases be wrong. With a fixed vertical resolution, we find simulations on anisotropic grids to capture the anisotropic nature of the turbulence better than simulations on isotropic grids. As indicated by the spectral energy densities shown in Figures 9b and 9d, the turbulence near the cloud top is more anisotropic in $A_{35,15}$ than in $A_{15,15}$. The coarser horizontal grid spacing in $A_{35,15}$ leads to higher effective viscosity in this direction which dampens vertical velocity fluctuations (e.g., as illustrated in Figure 4), and thereby mimics the observed anisotropy of stably stratified small-scale turbulence.

To sum up, we find that the observed cloud cover fraction of $\sim$1 is quite easily obtained by simply using a sufficiently high grid aspect ratio, e.g. $\Delta x/\Delta z=105/15=7$; it does not require a very fine vertical resolution. $\mathrm{LWP}^* \geq 1$ is more difficult to obtain. With $\Delta z=15$ m the increase in LWP^* with Δx seems to stop at $\Delta x \simeq 85$ m where $\mathrm{LWP}^* \simeq 0.7$. However by a small decrease of Δz to 10 m, $\mathrm{LWP}^* \simeq 1$ is obtained with $\Delta x=70$ m, and we get $\mathrm{LWP}^* > 1$ with $\Delta x=105$ m. With $\Delta z=5$ m the vertical extent of a typical STBL inversion layer will be resolved with a few grid points, and we find $\mathrm{LWP}^* \geq 1$ for all three values of Δx used here. We do however still see a strong dependence on the horizontal grid spacing, and speculate—based on the observed trend of the performed simulations—that reducing it to 5 m will result in the same low values of LWP^* as in $A_{15,15}$ and $A_{10,10}$, in poor agreement with observations. We hypothesize, that for simulations using isotropic grid boxes to agree well with observations, the grid spacing must be equal to or less than the cloud-top Ozmidov scale, or as suggested by *Khani and Waite* [2014] a fraction of the cloud-top bouyancy scale l_b. Using the Smagorinsky SGS model, *Khani and Waite* [2014] find that the grid spacing should be less than $0.17l_b$ which based on the POST data (Jen-La Plante et al., submitted manuscript, 2016) corresponds to $\sim 6L_O$, i.e., typically around 2.5 m. Regarding the profiles of $\langle w'w' \rangle$, none of the performed simulations in the present study come satisfyingly close to the measurements. Simulations with $\Delta z=5$ m do however perform significantly better than simulations with $\Delta z=10$ m and $\Delta z=15$ m. They are also the only ones—together with $A_{105,10}$—to reproduce the clearly negative values of $\langle w'w'w' \rangle$ observed in the cloud layer; i.e., we find that a downdraft-dominated cloud layer can be achieved by either using moderate grid aspect ratios and $\Delta z=5$ m, or high grid aspect ratios and $\Delta z=10$ m.

Within the parameter space studied here, we find domain size to have no significant impact on cloud statistics (such as the cloud cover and $\langle \mathrm{LWP} \rangle$). Visual inspection of horizontal cross sections through the subcloud and cloud layers indicate that the horizontal organization of updrafts and downdrafts does not depend on domain size, regardless of the resolution. We do, however, find the horizontal extent of the largest coherent updrafts to increase when the domain size is increased from $3.5\times3.5\times1.5\,\mathrm{km}^3$ to $7\times7\times1.5\,\mathrm{km}^3$ and to $14\times14\times1.5\,\mathrm{km}^3$. Further increase to $21\times21\times1.5\,\mathrm{km}^3$ shows little or no increase of the updraft size, indicating that a domain size of $14\times14\times1.5\,\mathrm{km}^3$ is sufficient in this case to account for the largest relevant flow

structures. However, we cannot exclude that longer simulation periods than the 6 h used here may result in larger structures requiring larger domains. Spectral analysis of the potential temperature from simulations $D_{85,15}$ and $D_{35,35}$ indicates that accurate simulation may require a domain with a horizontal extent larger than 21×21 km^2.

We show that the differences in $\langle$LWP$\rangle$ and cloud cover among simulations with different spatial resolution arise during the first 2 h of the simulation time. These initial changes in cloud structure immediately affect the cloud-top radiative cooling which in turn affect not only entrainment, but the dynamics of the STBL in general. This does not mean, however, that the observed differences between simulations are purely spin-up phenomena. We find that a simulation with $\Delta x=a$ initialized using interpolated fields (velocity, temperature etc.) from, say, 4 h of a simulation with $\Delta x=b > a$ gradually adjusts $\langle$LWP$\rangle$ and cloud cover back to values matching those from a simulation with grid spacing $\Delta x=a$ initialized according to the horizontally uniform profiles given by equations (1)–(4).

Finally we note that the results and conclusions presented here apply to the specific marine stratocumulus case. Simulation of other cases, e.g. with a broken cloud field and significant horizontal entrainment through the lateral cloud boundaries, may very well exhibit different dependencies on resolution and domain size.

Our choice to use ILES is motivated by the promising results of *Stevens et al*. [2005], *Piotrowski et al*. [2009], *Kurowski et al*. [2009], and *Remmler and Hickel* [2012]. We furthermore note that, in contrast to the traditional Smagorinsky-type SGS-modeling, ILES does not require specification of a single length scale based on grid spacings in all three directions, for instance, as $L_{sgs}=(\Delta x\Delta y\Delta z)^{1/3}$. Such a specification arguably leads to an overestimation of the vertical transport in simulations with anisotropic grids (e.g., compare results from LES with SGS terms included and ILES in Table A.I in *Kurowski et al*. [2009]). For future studies of the STBL, we are considering application of either a dynamic SGS model motivated by results of *Basu and Porté-Agel* [2006] and *Khani and Waite* [2015] or a generalized Smagorinsky model in the spirit of *Scotti et al*. [1993] to more properly account for the grid anisotropy. The method of ILES is still not fully mature, and it would be interesting to see if the results presented here could be reproduced using the more mature and widely accepted method of conventional LES.

The simplicity of the ILES model applied in this study made it possible to run all the performed simulations on a desktop computer within a reasonable amount of time. The results provide useful insights into the role of grid anisotropy in numerical simulation of the STBL and will be used in the setup of simulations of higher resolution and larger domain size.

Acknowledgments
This research was supported by Polish National Science Centre, grant agreement 2013/08/A/ST10/00291. NCAR is sponsored by the U.S. National Science Foundation. We would like to thank the two anonymous reviewers for their constructive comments. The ILES data presented in this paper can be obtained from the corresponding author upon request.

References

Basu, S., and F. Porté-Agel (2006), Large-eddy simulation of stably stratified atmospheric boundary layer turbulence: A scale-dependent dynamic modeling approach, *J. Atmos. Sci.*, *63*, 2074–2091.

Bryan, G. H., J. C. Wyngaard, and J. M. Fritsch (2003), Resolution requirements for the simulation of deep moist convection, *Mon. Weather Rev.*, *131*, 2394–2416.

Cheng, A., K.-M. Xu, and B. Stevens (2010), Effects of resolution on the simulation of boundary-layer clouds and the partition of kinetic energy to subgrid scales, *J. Adv. Model. Earth Syst.*, *2*, 3, doi:10.3894/JAMES.2010.2.3.

Chung, D., and G. Matheou (2014), Large-eddy simulation of stratified turbulence. Part I: A vortex-based subgrid-scale model, *J. Atmos. Sci.*, *71*, 1863–1879.

Clark, T. L., and R. D. Farley (1984), Severe downslope windstorm calculations in two and three spatial dimensions using anelastic interactive grid nesting: A possible mechanism for gustiness, *J. Atmos. Sci.*, *41*, 329–350.

Connolly, P. J., G. Vaughan, P. Cook, G. Allen, H. Coe, T. W. Choularton, C. Dearden, and A. Hill (2013), Modelling the effects of gravity waves on stratocumulus clouds observed during VOCALS-UK, *Atmos. Chem. Phys.*, *13*, 7133–7152.

Deardorff, J. W. (1980), Stratocumulus-capped mixed layers derived from a three-dimensional model, *Boundary Layer Meteorol.*, *18*, 495–527.

de Lozar, A., and J. P. Mellado (2013), Direct numerical simulations of a smoke cloud–top mixing layer as a model for stratocumuli, *J. Atmos. Sci.*, *70*, 2356–2375.

de Lozar, A., and J. P. Mellado (2015), Mixing driven by radiative and evaporative cooling at the stratocumulus top, *J. Atmos. Sci.*, *72*, 4681–4700.

de Roode, S. R., P. G. Duynkerke, and H. J. J. Jonker (2004), Large-eddy simulation: How large is large enough?, *J. Atmos. Sci.*, *61*, 403–421.

de Roode, S. R., I. Sandu, J. J. van der Dussen, A. S. Ackerman, P. Blossey, D. Jarecka, A. Lock, A. P. Siebesma, and B. Stevens (2016), Large eddy simulations of EUCLIPSE/GASS Lagrangian stratocumulus to cumulus transitions: Mean state, turbulence, and decoupling, *J. Atmos. Sci.*, doi:10.1175/JAS-D-15-0215.1, in press.

Domaradzki, J. A., Z. Xiao, and P. K. Smolarkiewicz (2003), Effective eddy viscosities in implicit large eddy simulations of turbulent flows, *Phys. Fluids*, *15*, 3890–3893.

Gerber, H., G. Frick, S. P. Malinowski, H. Jonsson, D. Khelif, and S. K. Krueger (2013), Entrainment rates and microphysics in POST stratocumulus, *J. Geophys. Res. Atmos.*, *118*, 12,094–12,109, doi:10.1002/jgrd.50878.

Germano, M., U. Piomelli, P. Moin, and W. H. Cabot (1991), A dynamic subgrid-scale eddy viscosity model, *Phys. Fluids A*, *3*, 1760–1765.
Grabowski, W. W. (2014), Extracting microphysical impacts in large-eddy simulations of shallow convection, *J. Atmos. Sci.*, *71*, 4493–4499.
Grabowski, W. W. (2015), Untangling microphysical impacts on deep convection applying a novel modeling methodology, *J. Atmos. Sci.*, *72*, 2446–2464.
Grabowski, W. W., and D. Jarecka (2015), Modeling condensation in shallow nonprecipitating convection, *J. Atmos. Sci.*, *72*, 4661–4679.
Grabowski, W. W., and P. K. Smolarkiewicz (1990), Monotone finite-difference approximations to the advection-condensation problem, *Mon. Weather Rev.*, *118*, 2082–2098.
Grabowski, W. W., and P. K. Smolarkiewicz (2002), A multiscale anelastic model for meteorological research, *Mon. Weather Rev.*, *130*, 939–956.
Grinstein, F. F., L. G. Margolin, and W. J. Rider (2007), *Implicit Large Eddy Simulation: Computing Turbulent Fluid Dynamics*, Cambridge Univ. Press, N. Y.
Haman, K. E., S. P. Malinowski, M. J. Kurowski, H. Gerber, and J.-L. Brenguier (2007), Small scale mixing processes at the top of a marine stratocumulus—A case study, *Q. J. R. Meteorol. Soc.*, *133*, 213–226.
Heinze, R., D. Mironov, and S. Raasch (2015), Second-moment budgets in cloud topped boundary layers: A large-eddy simulation study, *J. Adv. Model. Earth Syst.*, *7*, 510–536, doi:10.1002/2014MS000376.
Jones, C. R., C. S. Bretherton, and P. N. Blossey (2014), Fast stratocumulus time scale in mixed layer model and large eddy simulation, *J. Adv. Model. Earth Syst.*, *6*, 206–222, doi:10.1002/2013MS000289.
Katzwinkel, J., H. Siebert, and R. A. Shaw (2012), Observation of a self-limiting, shear-induced turbulent inversion layer above marine stratocumulus, *Boundary Layer Meteorol.*, *145*, 131–143.
Khani, S., and M. L. Waite (2014), Buoyancy scale effects in large-eddy simulations of stratified turbulence, *J. Fluid Mech.*, *754*, 75–97.
Khani, S., and M. L. Waite (2015), Large eddy simulations of stratified turbulence: The dynamic smagorinsky model, *J. Fluid Mech.*, *773*, 327–344.
Kurowski, M. J., S. P. Malinowski, and W. W. Grabowski (2009), A numerical investigation of entrainment and transport within a stratocumulus-topped boundary layer, *Q. J. R. Meteorol. Soc.*, *135*, 77–92.
Kurowski, M. J., W. W. Grabowski, and S. P. Malinowski (2010), Impact of radiative cooling and subgrid-scale mixing on the evolution of stratocumulus-topped boundary layer, in *13th AMS Conference on Cloud Physics*, Portland, OR. [Available at https://ams.confex.com/ams/pdfpapers/171684.pdf.]
Kurowski, M. J., W. W. Grabowski, and P. K. Smolarkiewicz (2014), Anelastic and compressible simulation of moist deep convection, *J. Atmos. Sci.*, *71*, 3767–3787.
Lindborg, E. (2006), The energy cascade in a strongly stratified fluid, *J. Fluid Mech.*, *550*, 207–242.
Malinowski, S. P., H. Gerber, I. J.-L. Plante, M. K. Kopec, W. Kumala, K. Nurowska, P. Y. Chuang, D. Khelif, and K. E. Haman (2013), Physics of Stratocumulus Top (POST): Turbulent mixing across capping inversion, *Atmos. Chem. Phys.*, *13*, 12,171–12,186.
Margolin, L. G., and W. J. Rider (2002), A rationale for implicit turbulence modelling, *Int. J. Numer. Methods Fluids*, *39*, 821–841.
Matheou, G., and D. Chung (2014), Large-eddy simulation of stratified turbulence. Part II: Application of the stretched-vortex model to the atmospheric boundary layer, *J. Atmos. Sci.*, *71*, 4439–4460.
Moeng, C.-H., et al. (1996), Simulation of a stratocumulus-topped planetary boundary layer: Intercomparison among different numerical codes, *Bull. Am. Meteorol. Soc.*, *77*, 261–278.
Nishizawa, S., H. Yashiro, Y. Sato, Y. Miyamoto, and H. Tomita (2015), Influence of grid aspect ratio on planetary boundary layer turbulence in large-eddy simulations, *Geosci. Model Dev.*, *8*, 3393–3419, doi:10.5194/gmd-8-3393-2015.
Pedersen, J. G., S.-E. Gryning, and M. Kelly (2014), On the structure and adjustment of inversion-capped neutral atmospheric boundary-layer flows: Large-eddy simulation study, *Boundary Layer Meteorol.*, *153*, 43–62.
Peltier, L. J., J. C. Wyngaard, S. Khanna, and J. G. Brasseur (1996), Spectra in the unstable surface layer, *J. Atmos. Sci.*, *53*, 49–61.
Piotrowski, Z. P., P. K. Smolarkiewicz, S. P. Malinowski, and A. A. Wyszogrodzki (2009), On numerical realizability of thermal convection, *J. Comput. Phys.*, *228*, 6268–6290.
Prusa, J. M., P. K. Smolarkiewicz, and A. A. Wyszogrodzki (2008), EULAG, a computational model for multiscale flows, *Comput. Fluids*, *37*, 1193–1207.
Remmler, S., and S. Hickel (2012), Direct and large eddy simulation of stratified turbulence, *Int. J. Heat Fluid Flow*, *35*, 13–24.
Scotti, A., C. Meneveau, and D. K. Lilly (1993), Generalized Smagorinsky model for anisotropic grids, *Phys. Fluids A*, *5*, 2306–2308.
Smagorinsky, J. (1963), General circulation experiments with the primitive equations, *Mon. Weather Rev.*, *91*, 99–164.
Smolarkiewicz, P. K. (1984), A fully multidimensional positive definite advection transport algorithm with small implicit diffusion, *J. Comput. Phys.*, *54*, 325–362.
Smolarkiewicz, P. K. (2006), Multidimensional positive definite advection transport algorithm: An overview, *Int. J. Numer. Methods Fluids*, *50*, 1123–1144.
Song, K., and S. S. Yum (2012), Anthropogenic radiative forcing of marine stratocumulus clouds under different thermodynamic conditions—an LES model study, *Atmos. Res.*, *118*, 370–389.
Stevens, B. (2000), Cloud transitions and decoupling in shear-free stratocumulus-topped boundary layers, *Geophys. Res. Lett.*, *27*, 2557–2560.
Stevens, B., et al. (2003), Dynamics and chemistry of marine stratocumulus—DYCOMS-II, *Bull. Am. Meteorol. Soc.*, *84*, 579–593.
Stevens, B., et al. (2005), Evaluation of large-eddy simulations via observations of nocturnal marine stratocumulus, *Mon. Weather Rev.*, *133*, 1443–1462.
Stevens, D. E., A. S. Ackerman, and C. S. Bretherton (2002), Effects of domain size and numerical resolution on the simulation of shallow cumulus convection, *J. Atmos. Sci.*, *59*, 3285–3301.
Sullivan, P. P., and E. G. Patton (2011), The effect of mesh resolution on convective boundary layer statistics and structures generated by large-eddy simulation, *J. Atmos. Sci.*, *68*, 2395–2415.
van der Dussen, J. J., S. R. de Roode, S. D. Gesso, and A. P. Siebesma (2015), An LES model study of the influence of the free tropospheric thermodynamic conditions on the stratocumulus response to a climate perturbation, *J. Adv. Model. Earth Syst.*, *7*, 670–691, doi:10.1002/2014MS000380.
Wood, R. (2012), Stratocumulus Clouds, *Mon. Weather Rev.*, *140*, 2373–2423.
Wood, R., and D. L. Hartmann (2006), Spatial variability of liquid water path in marine low cloud: The importance of mesoscale cellular convection, *J. Clim.*, *19*, 1748–1764.
Yamaguchi, T., and G. Feingold (2012), Technical note: Large-eddy simulation of cloudy boundary layer with the Advanced Research WRF model, *J. Adv. Model. Earth Syst.*, *4*, M09003, doi:10.1029/2012MS000164.
Yamaguchi, T., and D. A. Randall (2012), Cooling of entrained parcels in a large-eddy simulation, *J. Atmos. Sci.*, *69*, 1118–1136.
Yamaguchi, T., W. A. Brewer, and G. Feingold (2013), Evaluation of modeled stratocumulus-capped boundary layer turbulence with shipborne data, *J. Atmos. Sci.*, *70*, 3895–3919.